

QUANTIFYING T CELL MORPHODYNAMICS AND MIGRATION IN 3D COLLAGEN MATRICES

YEEREN I. LOW

Department of Physics, McGill University, Montréal, Québec, Canada

ABSTRACT. T cells undergo large shape changes (morphodynamics) when migrating. While progress has been made elucidating the molecular basis of cell migration, statistical characterization of morphodynamics and migration has been limited, particularly in physiologically realistic 3D environments. A previous study (H. Cavanagh *et al.*, *J. R. Soc. Interface* **19**: 20220081) found discrete states of dynamics as well as periodic oscillations of shape. However, we show that these results are due to artifacts of the analysis methods. Here, we present a revised analysis of the data, applying a method based on an underdamped Langevin equation. We find that different shape modes have different correlation times. We also find novel non-Gaussian effects. This study provides a framework in which quantitative comparisons of cell morphodynamics and migration can be made, e.g. between different biological conditions or mechanistic models.

1. INTRODUCTION

Efficient migration of leukocytes (immune cells) is crucial to mounting an effective immune response. Leukocytes must travel through various microenvironments in order to scan tissues for targets such as pathogens, antigen, or other cells [1].

Cell migration depends fundamentally on remodeling of the actin cytoskeleton. Leukocyte migration can occur spontaneously or as a result of extracellular cues such as chemokine, and is enabled by protrusion of pseudopods containing a branched actin network at the front and contraction of actomyosin bundles at the back [2], occurring in some contexts as a cyclical process [3]. It has been proposed that actin protrusions play an exploratory role but are dispensable for migration [4, 5]. Meanwhile, an actin cortex maintains the integrity of the cell shape. The cells have a polarized shape, with a rounded or wide cell front while the cell rear contains a thin cylindrical structure called the uropod [6]. Membrane material for large shape changes is provided by microvilli, which cover the cells [7].

Leukocytes utilize a fast mode migration termed “amoeboid”, so named due to their large shape changes and similarity to the social amoeba *Dictyostelium discoideum* [8]. This migration mode is further characterized by weak adhesion and typically does not involve proteolysis of the extracellular matrix [9–11]. While many studies have analyzed cell migration in 2D, it is more physiologically realistic to consider 3D migration [12]. On 2D surfaces, leukocytes use adhesion receptors (such as integrins) to anchor the cell during protrusion [13]; however, in 3D environments they are able to use an adhesion-independent mode of migration, using a “flowing and squeezing” mechanism instead

E-mail address: yeeren.low@mail.mcgill.ca.

[14], and they are also able to use topography to generate motion [15]. However, determination of the actual mechanism underlying migration is complicated by adaptability [10].

Leukocyte migration can be characterized as a search problem, and different types of random walks have been proposed to describe it [16]. Migration is modulated by both environmental and cell-intrinsic factors [17–19], and molecular perturbations are seen to modify turning behavior [20, 21].

Turning to the underpinnings of cell locomotion, actin waves have been observed in a variety of cell types and are thought to underlie cell migration. They are hypothesized to arise from an excitable system [22, 23]. Membrane tension is proposed to act as a global negative feedback to restrict protrusive activity around the cell surface [24]. In 2D migration of the social amoeba *Dictyostelium discoideum*, the molecular workings of the excitable system have been recently elucidated [25–29]. For cell migration more generally, there have been significant modeling efforts, particularly in the case of 2D migration [30–35]. Modeling biochemical reactions along with cellular shape change, however, poses particular challenges due to the so-called “moving boundary problem” [36, 37]. Swimming in 3D of *Dictyostelium* has been modeled by a reaction-diffusion system on the membrane [38]. Both 2D crawling and 3D swimming of *Dictyostelium* occur by protrusions forming at the front of the cell, which bifurcate and translocate toward the rear of the cell [39–42]. These shape changes are time-irreversible in accordance with Purcell’s scallop theorem [43], although shape changes are not strictly required for swimming [44, 45]. Time-irreversible force dynamics has also been observed for 3D mesenchymal migration [46]. Meanwhile, links between cell shape and migration have been studied [47]. The connection between biology and mechanics is known as mechanobiology, which is a growing field [48].

To model cellular shape change and migration, rather than taking a “bottom-up” or mechanistic approach to modeling, where biochemical reactions are posited and force balance equations are written, we opt for a “top-down” or data-driven approach, where experimental data is characterized by measured statistical coefficients. This approach allows for identification of important quantities governing the dynamics, which could be compared between different biological conditions or used as benchmarks for mechanistic models. In the words of [49], such characterization “is important because it defines the motion that the bottom-up approach attempts to explain”. Data-driven modeling of cell migration has been done mostly in 2D [49–62]. Similar methods have been used to characterize dynamics of the nematode worm *Caenorhabditis elegans* shape and motion [63–73] and cell migration confined to adhesive micropatterns [74–78]. A review of top-down modeling efforts applied to cell migration is given in [79].

T cell morphodynamics and migration in 3D collagen matrices have been previously analyzed in [80]. However, that study contains several major flaws and shortcomings which will be discussed in the main text. This paper presents a reanalysis of the data in [80].

2. DIMENSIONALITY REDUCTION OF THE SHAPE OF MOTILE CELLS

First, motile cells were distinguished from sessile cells based on trajectories of the cell centroid. Due to the small number of cells measured, this could be done manually, with the trajectories of motile cells spanning a distance (the maximum distance between two points on a trajectory) of at least $\approx 20 \mu\text{m}$. A total of 10 motile cells were detected, all recorded with a frame interval of 4.17 s.

Next, we analyzed the shapes of the motile cells. Sessile cells are spherical, whereas motile cells assume a polarized shape [81]. The study [80] uses descriptors of the cell surface based on spherical harmonics Y_l^m , and taking for each value of l the squared magnitude summed over m . However, this loses information. The study [80] partially remedies this by tracking the uropod and recording

the distance between the uropod and centroid. We can do better by taking moments of harmonic polynomials relative to the uropod-centroid axis; we use this axis as a proxy for the polarization axis. We use a convention for Y_l^m without Condon–Shortley phase, where:

$$(1) \quad \frac{1}{4\pi} \int d\Omega Y_l^m Y_{l'}^{m'*} = \delta_{ll'} \delta_{mm'}.$$

We define central moments:

$$(2) \quad M_l^m := \int d\mathcal{A} r^l Y_l^m(\theta, \phi),$$

where r is the distance from the cell centroid to a point on the surface, and normalized moments:

$$(3) \quad m_l^m := \frac{M_l^m}{\mathcal{A}^{(l+2)/2}},$$

where \mathcal{A} is the cell surface area. Due to translational symmetry, there are no $l = 1$ terms. Rotational invariance is broken by the choice of polarization axis. The next question is how to scale the quantities with different values of l . We consider a small deviation from a spherical surface, represented by $r = R(1 + \epsilon_l^m Y_l^m)$ for some constant R (using real spherical harmonics¹). For $l \geq 2$, to order $\mathcal{O}(\epsilon_l^m)$, we have:

$$(4) \quad m_l^m = \frac{l+2}{(4\pi)^{l/2}} \epsilon_l^m.$$

Thus, we define our shape variables s_l^m as:

$$(5) \quad s_l^m := \frac{(4\pi)^{l/2}}{l+2} m_l^m,$$

for $l \geq 2$. For $l = 0$, we define $s_0^0 := \log(\mathcal{A}/4\pi)/2$ so that a change $r \rightarrow (1 + \epsilon)r$ results in a corresponding change $s_0^0 \rightarrow s_0^0 + \epsilon$. In addition, if the uropod-centroid axis is called the z -axis, we define components of the velocity $v^0 := v^z$ and $v^1 := v^x + iv^y$, as well as orientational changes $\Delta\theta e^{i\phi}$.

Lastly, we use principal component analysis, but before doing so, we subtract the cell-wise mean of the shape parameters. Without doing so, we may obtain a situation where the first principal component mainly reflects population variability [82]. We retain moments up to order $l = 3$, as this is the minimal possible value of l for which amoeboid swimming by means of shape change is possible [83]. The $l = 2, m = 0$ mode is simply elongation of the cell along its axis (the z -axis). The $l = 2, m = 1$ mode describes tilting of the cell and is positive when the cell front ($z > 0$) deviates in the $+x$ -direction while the cell back ($z < 0$) deviates in the $-x$ -direction. The $l = 2, m = 2$ mode describes lateral elongation of the cell and is positive when the elongation is along the x -axis. The $l = 3, m = 0$ mode describes broken symmetry along the polarization axis and is positive when the cell front is narrower than the cell back. Thus the “stereotypical” shape of a polarized cell, which is wide at the front, has $s_3^0 < 0$. The $l = 3, m = 1$ mode describes a bent shape, and is positive when the front and back of the cell deviate in the $+x$ -direction while in between it deviates in the $-x$ -direction. The $l = 3, m = 2$ mode describes differential lateral elongation, and positive when the front of the cell is elongated along the x -axis while the back of the cell is elongated along the y -axis. The $l = 3, m = 3$ mode describes a triangular deformation

¹For $m > 0$, the use of real spherical harmonics leads to a factor of $\sqrt{2}$ in the definition of ϵ_l^m relative to complex spherical harmonics. If we refer to the coefficients of real spherical harmonics as $\Re\epsilon_l^m$ and $\Im\epsilon_l^m$, as we do here, then the squared magnitude of the deformation mode is $|\epsilon_l^m|^2$ rather than $2|\epsilon_l^m|^2$.

TABLE 1. Quantities with 95% confidence intervals.

$\exp(\langle s_0^0 \rangle)$	$9.2 \pm 0.8 \text{ } \mu\text{m}$
$\langle s_2^0 \rangle$	0.16 ± 0.07
$\langle s_3^0 \rangle$	-0.12 ± 0.03
$\langle v^0 \rangle$	$0.28 \pm 0.08 \text{ } \mu\text{m}/\text{fr}$
$\text{Var}(s_0^0)$	$(1.1 \pm 0.8) \times 10^{-3}$
$\text{Var}(s_2^0)$	$(5.6 \pm 2.2) \times 10^{-3}$
$\langle s_2^1 s_2^{1*} \rangle$	$(8.7 \pm 2.8) \times 10^{-3}$
$\langle s_2^2 s_2^{2*} \rangle$	$(6.7 \pm 2.1) \times 10^{-3}$
$\text{Var}(s_3^0)$	$(2.8 \pm 1.1) \times 10^{-3}$
$\langle s_3^1 s_3^{1*} \rangle$	$(3.2 \pm 1.4) \times 10^{-3}$
$\langle s_3^2 s_3^{2*} \rangle$	$(2.2 \pm 1.0) \times 10^{-3}$
$\langle s_3^3 s_3^{3*} \rangle$	$(0.8 \pm 0.5) \times 10^{-3}$
$\text{Cov}(s_2^0, s_3^0)$	$(-1.0 \pm 1.1) \times 10^{-3}$
$\langle s_2^1 s_3^{1*} \rangle$	$(1.1 \pm 0.7) \times 10^{-3} + (0.2 \pm 0.8) \times 10^{-3}i$
$\langle s_2^2 s_3^{2*} \rangle$	$(2.6 \pm 1.0) \times 10^{-3} + (0.1 \pm 0.3) \times 10^{-3}i$

in the xy -plane, and is positive when the shape is elongated along the $(1, 0)$ and $(-1/2, \pm\sqrt{3}/2)$ directions. In Table 1, 95% confidence intervals calculated using a t -distribution are listed. The only non-zero quantities are invariant under a change of definition of azimuth $\phi \rightarrow \phi + \Delta\phi$, due to symmetry in the description. We see that the variance of the volume variable s_0^0 is small compared to the principal shape variables, and the variance of s_3^3 is also small. We also see that, up to this point in the analysis, there is no chirality, which would be manifested as symmetry $\phi \rightarrow -\phi$ being broken.

Next, we investigate whether dynamics is stationary. We will see later that a description based on overdamped Langevin equations [84] is not sufficient on the measured time-scales, i.e., an underdamped description [85] is necessary.² We use the characterization based on second-order time-symmetric and -antisymmetric quantities [87] and perform linear regression of these quantities with respect to time. Before statistical analysis, we also scale each cell's quantities by a suitable factor related to the cell-wise variances of the variables. Using a t -test with Holm–Bonferroni correction, no statistically significant deviation from stationarity was detected.

²Non-Markovianity of cell shapes in 2D for measurements with a 3 s frame interval was suggested in [86]. However, quantities were linearly interpolated between time-points, which is expected to introduce artificial non-Markovianity.

3. LINEAR GAUSSIAN MODEL

Here, we fit a linear Gaussian model to the dynamics. In such a model, only quantities with the same (absolute value of) m can couple to each other. For $m = 0$, the model is:

$$(6) \quad \begin{pmatrix} \dot{s}_2^0 \\ \dot{s}_3^0 \\ \dot{v}^0 \end{pmatrix} = \mathbf{A}_x^0 \Delta \mathbf{s}_{2:3}^0 + \mathbf{A}_v^0 \begin{pmatrix} \dot{s}_2^0 \\ \dot{s}_3^0 \\ \Delta v^0 \end{pmatrix} + \boldsymbol{\xi}^0, \quad \langle \boldsymbol{\xi}^0(t) \rangle = \mathbf{0}, \quad \langle \boldsymbol{\xi}^0(t) \boldsymbol{\xi}^0(t')^\top \rangle = 2\mathbf{D}^0 \delta(t - t'),$$

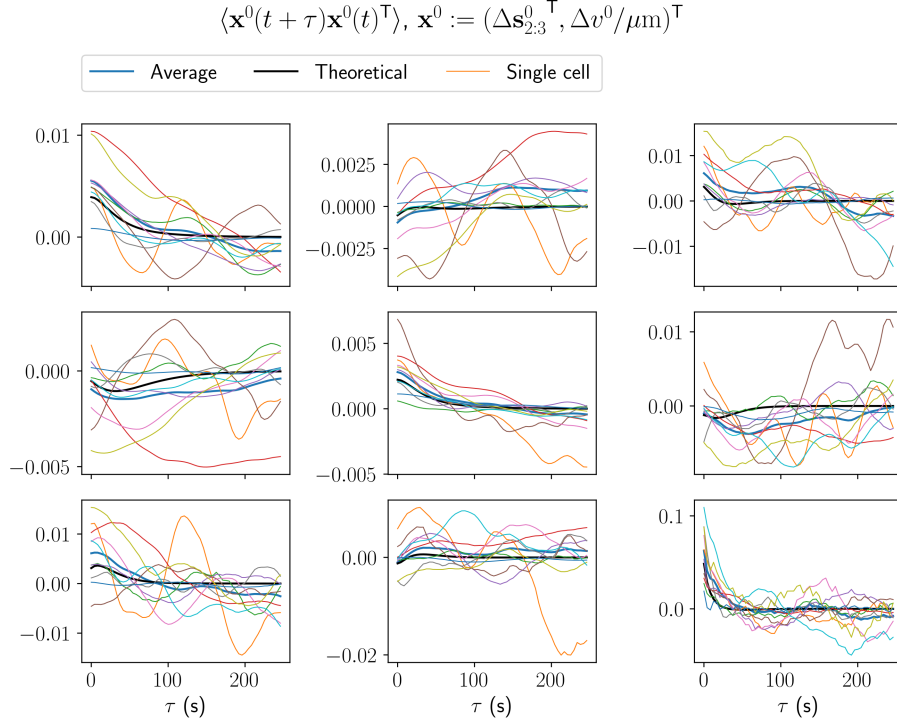
where Δ denotes deviation from the cell-wise mean, and $\mathbf{s}_{2:3}^0 := (s_2^0, s_3^0)^\top$. We used the procedure described in [85] to infer dynamics; however, we found it to be necessary to fit a continuous-time model exactly (see Appendix A). We compared the measured and theoretical covariance functions, with good agreement (Fig. 1). We see that on relatively long time-scales ($\gtrsim 30$ s), the shape autocovariances decay exponentially. We computed a decay rate of $0.019 \pm 0.010 \text{ s}^{-1}$ (95% confidence interval, t -distribution) corresponding to a correlation time of 51 s. Next, we used the characterization based on time-symmetric and -antisymmetric quantities [87], and scaled each cell's quantities by a suitable factor related to the variances, e.g. $\langle \Delta s_2^0 \Delta s_3^0 \rangle / (\langle (\Delta s_2^0)^2 \rangle \langle (\Delta s_3^0)^2 \rangle)^{1/2}$. We used a t -test with Holm–Bonferroni correction to evaluate statistical significance.³ We evaluated quantitative significance of effects using the procedure described in [87] for the case of almost-Markovian dynamics. For quantities involving fluctuations (diffusivities), we do the comparison using the discrete-time estimators described in [85] (this is done throughout the paper). The quantities with both statistical and quantitative significance are $\langle \Delta s_2^0 \dot{s}_3^0 \rangle < 0$ (adjusted $p = 0.008$) and $L(\dot{s}_2^0, \dot{s}_3^0) < 0$ (adjusted $p = 1.4 \times 10^{-4}$) where $L(\cdot, \cdot)$ is the angular momentum [87]. This is in accordance with previous observations of time-irreversibility [39–42].

We now turn to the $m = 1$ dynamics, described by:

$$(7) \quad \begin{pmatrix} \dot{s}_2^1 \\ \dot{s}_3^1 \\ (d/dt)(\dot{\theta} e^{i\phi}) \\ \dot{v}^1 \end{pmatrix} = \mathbf{A}_x^1 \mathbf{s}_{2:3}^1 + \mathbf{A}_v^1 \begin{pmatrix} \dot{s}_2^1 \\ \dot{s}_3^1 \\ \dot{\theta} e^{i\phi} \\ v^1 \end{pmatrix} + \boldsymbol{\xi}^1, \quad \langle \boldsymbol{\xi}^1(t) \rangle = \mathbf{0}, \quad \langle \boldsymbol{\xi}^1(t) \boldsymbol{\xi}^1(t')^\text{H} \rangle = 2\mathbf{D}^1 \delta(t - t').$$

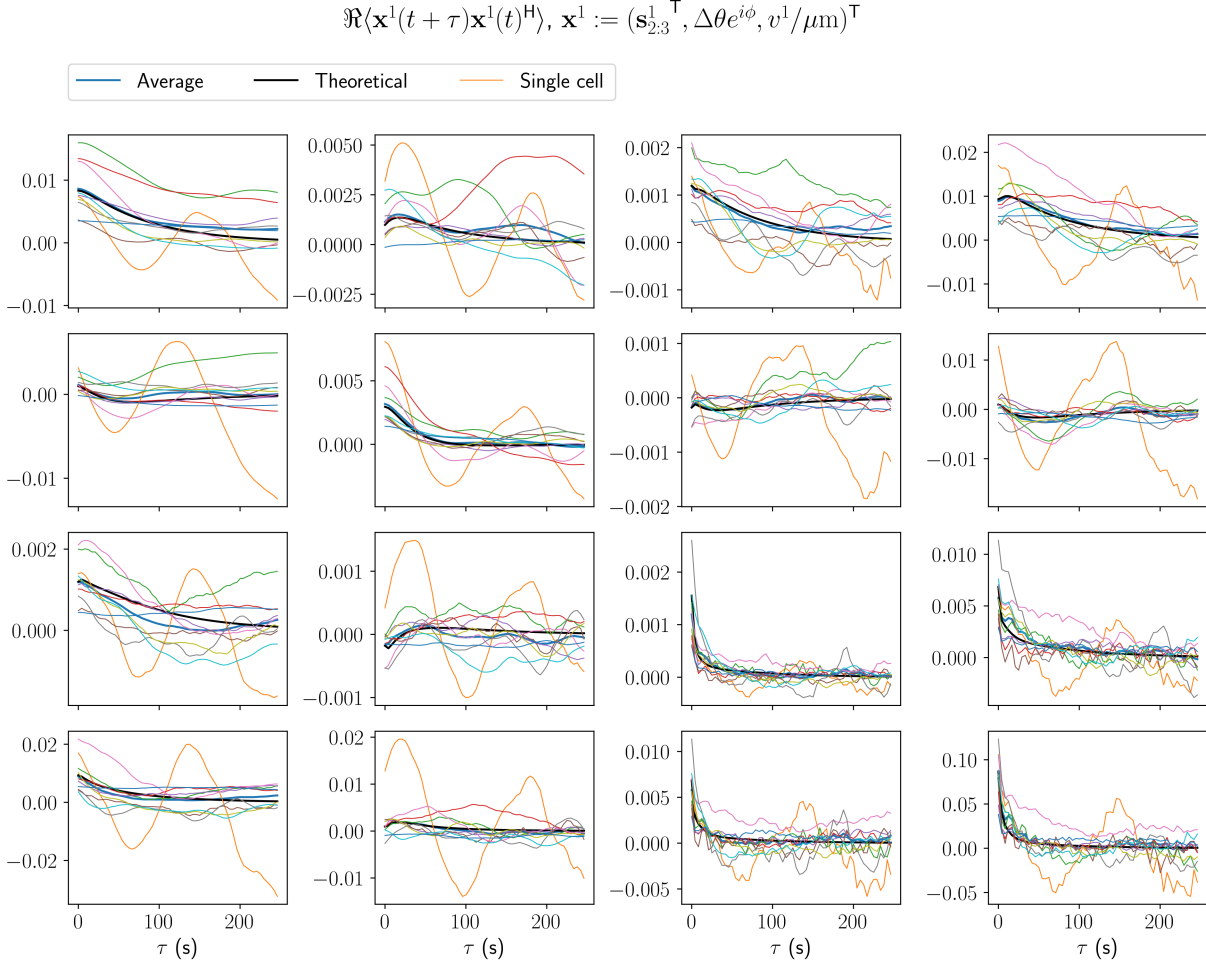
Now, we see a difference in the correlation times of s_2^1 and s_3^1 . We calculated decay rates of $0.014 \pm 0.006 \text{ s}^{-1}$ and $0.031 \pm 0.010 \text{ s}^{-1}$, corresponding to correlation times of 85 s and 27 s, again with good agreement between theory and experiment (Fig. 2). The smaller decay rate was always associated with an eigenvector with larger s_2^1 component. The statistically and quantitatively significant quantities are listed in Table 2. Again, we see time-irreversibility in the same sense as before. In addition, we have the time-antisymmetric quantities $\Re \langle s_2^1 \dot{\theta} e^{-i\phi} \rangle, \Re \langle s_2^1 v^{1*} \rangle > 0$. We also have correlated fluctuations $\Re D_{3\theta}^1, \Re D_{\theta v}^1 > 0$. As with $m = 0$, on long time-scales the shape autocovariances decay exponentially. In contrast with $m = 0$, we now have the possibility of

³Due to a population of only 10 cells, we opted for a t -test instead of a bootstrap [88]. The reason is that if 10 quantities are sampled i.i.d. from a distribution with median 0, then with probability 2^{-9} , all values will have the same sign. Thus, we cannot estimate p -values below 2^{-9} using the bootstrap. However, the Holm–Bonferroni correction demands estimation of such p -values, as will be seen. As for Gaussianity, while instantaneous quantities may not be normally distributed, we would expect that the time-average approximately obeys a Gaussian distribution. It may be objected that the Gaussian approximation does not hold at low p -values; however, other procedures might introduce either additional assumptions or greatly increased computational cost. Therefore, we settled on the procedure used here as a reasonable approximation.

FIGURE 1. Covariance functions with $m = 0$. Velocities are in units of $\mu\text{m}/\text{fr}$.TABLE 2. Statistically and quantitatively significant quantities for $m = 1$.

Quantity and sign	Adjusted p -value
$\Re\langle s_2^1 s_3^{1*} \rangle < 0$	0.012
$\Re\langle s_2^1 \dot{\theta} e^{-i\phi} \rangle > 0$	4.2×10^{-5}
$\Re\langle s_2^1 v^{1*} \rangle > 0$	1.4×10^{-3}
$\Re\langle \dot{\theta} e^{i\phi} v^{1*} \rangle > 0$	1.6×10^{-7}
$\Re L\langle \dot{s}_2^1, \dot{s}_3^{1*} \rangle < 0$	9.6×10^{-3}
$\Re L\langle \dot{\theta} e^{i\phi}, v^{1*} \rangle < 0$	1.4×10^{-3}
$\Re D_{3\theta}^1 > 0$	1.0×10^{-3}
$\Re D_{\theta v}^1 > 0$	5.0×10^{-5}

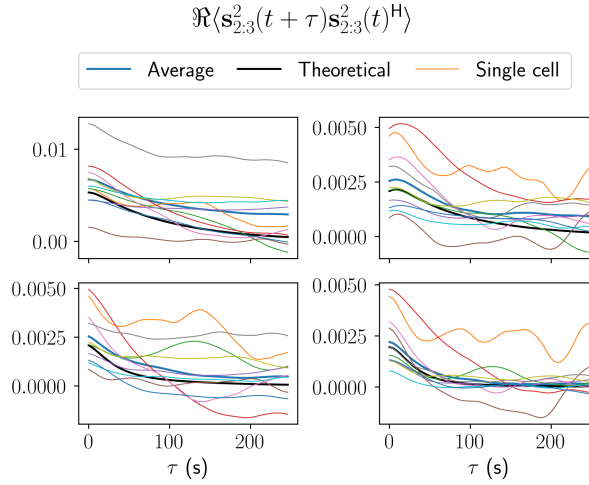
chirality. However, no chirality was detected. The imaginary part of the $m = 1$ covariance function was also null within statistical error (not shown).


 FIGURE 2. Covariance functions with $m = 1$. Velocities are in units of $\mu\text{m}/\text{fr}$.

Finally, we have the $m = 2$ dynamics, which is described by:

$$(8) \quad \ddot{\mathbf{s}}_{2:3}^2 = \mathbf{A}_{\mathbf{x}}^2 \mathbf{s}_{2:3}^2 + \mathbf{A}_{\mathbf{v}}^2 \dot{\mathbf{s}}_{2:3}^2 + \boldsymbol{\xi}^2, \quad \langle \boldsymbol{\xi}^2(t) \rangle = \mathbf{0}, \quad \langle \boldsymbol{\xi}^2(t) \boldsymbol{\xi}^2(t')^H \rangle = 2\mathbf{D}^2 \delta(t - t').$$

We again have a difference in the correlation times of s_2^2 and s_3^2 . We computed decay rates of $(8.8 \pm 6.0) \times 10^{-3} \text{ s}^{-1}$ and $0.040 \pm 0.017 \text{ s}^{-1}$, corresponding to correlation times of 99 s and 20 s, again with good agreement between theory and experiment (Fig. 3). The smaller decay rate was always associated with an eigenvector with larger s_2^2 component. Visually, there appears to be the possibility of correlations of s_2^2 to be longer-lived than predicted by theory. However, a statistical test conducted at $\tau = 209$ s gives a non-significant result of $p = 0.024$ when multiple hypotheses are taken into account. The statistically and quantitatively significant quantities are listed in Table 3, again with time-irreversibility in the same sense as before, and no chirality detected. As before, for

FIGURE 3. Covariance functions with $m = 2$.TABLE 3. Statistically and quantitatively significant quantities for $m = 2$.

Quantity and sign	Adjusted p -value
$\Re\langle s_2^2 s_3^{2*} \rangle > 0$	1.7×10^{-7}
$\Re\langle s_2^2 \dot{s}_3^{2*} \rangle < 0$	5.0×10^{-4}
$\Re\langle \dot{s}_2^2 \dot{s}_3^{2*} \rangle > 0$	4.2×10^{-7}
$\Re L(\dot{s}_2^2, \dot{s}_3^{2*}) < 0$	2.6×10^{-4}
$\Re D_{23}^2 > 0$	3.5×10^{-6}

long time-scales the autocovariances decay exponentially. Also, the imaginary part of the $m = 2$ covariance function was null within statistical error (not shown).

We may compare our results to diffusion on a sphere. The spherical Laplacian has eigenfunctions $Y_l^m(\theta, \phi)$ with eigenvalues $-l(l+1)$. We observe a difference in correlation times for $l = 2$ and $l = 3$ for $m > 0$, but not for $m = 0$.

4. PREVIOUS ANALYSIS

The previous study [80] claimed oscillatory autocovariance functions (ACFs) together with much longer correlation times (≥ 150 s). However, the power spectra (Supplementary Figure 5c in [80]) do not contain a peak at non-zero frequency. This suggests that the supposed oscillations in the ACFs are statistical noise. Thus, the fitting method which uses the peaks of the measured ACFs grossly overestimates the correlation times. A rough comparison of the power spectra of cells in the “run” mode to a Lorentzian function (the power spectrum of an Ornstein–Uhlenbeck process) suggests correlation times of approximately 60 s for all three principal components, in accordance with our results for the $m = 0$ modes. The results for the cells in the “stop” mode are suspect, as it

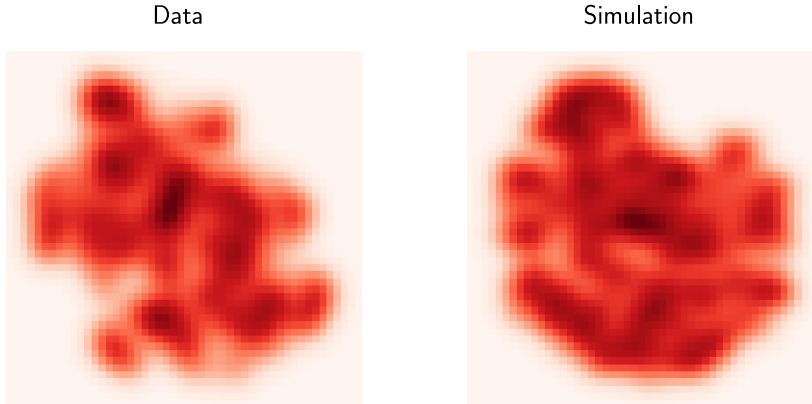


FIGURE 4. Probability distributions obtained from applying t-SNE to real data and simulated data from a linear Gaussian model.

is known that (and has been mentioned earlier that) sessile cells are spherical [81]. Indeed, manual inspection of the trajectories of the cell centroid reveals that two out of the four cells classified as “stop” in [80] are in fact motile.

Next, it was claimed that morphodynamics can be described as inhabiting a set of discrete states. This conclusion was reached by using wavelet analysis along with t-SNE. However, applying the t-SNE algorithm to finite data can result in artifactual non-uniform probability distributions. To test for this possibility, the analysis procedure was applied to the $m = 0$ shape variables and compared with the linear Gaussian model from the previous section simulated for 1764 frames (the same number of frames as in the dataset of motile cells), with very similar results (Fig. 4; also compare Supplementary Figure 9a in [80]). Thus, the appearance of multiple peaks in the probability distribution seems to be an artifact of t-SNE.

Next, in [80] it was claimed that the dynamics of the second principal component contain oscillations with period 100 s. However, as was mentioned earlier, there is no peak in the power spectra at non-zero frequency. This suggests a different explanation for the observed oscillations. The wavelet transform is obtained by convoluting the time-series with the wavelet, which means that the Fourier transforms of the time-series and the wavelet are multiplied. The maximum power of the first and second derivatives of a Gaussian with standard deviation σ occurs at angular frequencies of σ^{-1} and $\sqrt{2}\sigma^{-1}$, respectively. The so-called “width of influence” of the wavelet is taken to be approximately 6σ , according to the code provided in [80]. It was claimed that the entropy⁴ is minimized when the ratio of the width of the Mexican hat to the width of the derivative of a Gaussian is 1.5, while the oscillation frequency is located at the maximum of the power spectra of the wavelets. Together, these strongly support the explanation of oscillations as an artifact of the wavelet transform.

Lastly, because wavelets have zero integral, the analysis of dynamics in [80] removes information about location in shape space. In contrast, we analyze dynamics as a function of shape.

⁴Not to be confused with physical entropy production, which is related to the probability ratio between forward and backward trajectories [89].

5. NON-GAUSSIAN EFFECTS

Following [87], we characterize the third-order dynamics by the quantities $\langle x^i x^j x^k \rangle$, $\langle x^i x^j \dot{x}^k \rangle$ where:

$$(9) \quad \langle x^i x^j \dot{x}^k \rangle + \langle x^i \dot{x}^j x^k \rangle + \langle \dot{x}^i x^j x^k \rangle = 0,$$

$$\langle x^i \dot{x}^j \dot{x}^k \rangle,$$

$$(10) \quad \tilde{L}(x^i, \dot{x}^j, \dot{x}^k) := \frac{1}{2} [L(x^i \dot{x}^j, \dot{x}^k) - L(x^i \dot{x}^k, \dot{x}^j)],$$

$\langle \dot{x}^i \dot{x}^j \dot{x}^k \rangle$, and $L(\dot{x}^i \dot{x}^j, \dot{x}^k)$, where:

$$(11) \quad L(\dot{x}^i \dot{x}^j, \dot{x}^k) + L(\dot{x}^j \dot{x}^k, \dot{x}^i) + L(\dot{x}^k \dot{x}^i, \dot{x}^j) = 0.$$

⁵In the case of almost-Markovian dynamics, the first four sets of quantities form one group, while the last two sets of quantities form another group [87]. For our system, in the first group, there are 389 independent quantities, of which 75 are purely real and 12 are purely imaginary. In the second group, there are 338 independent quantities, of which 72 are purely real and none are purely imaginary. We apply Holm–Bonferroni correction independently to each group and evaluate quantitative significance according to [87]. As before, prior to statistical testing, we divide quantities for each cell by a factor related to the variances (e.g. $\langle \Delta s_i^0 \Delta s_j^0 \Delta s_k^0 \rangle / (\langle (\Delta s_i^0)^2 \rangle \langle (\Delta s_j^0)^2 \rangle \langle (\Delta s_k^0)^2 \rangle)^{1/2}$). As with the second-order quantities, we tested these for trends but found nothing statistically significant. We estimate the contribution of measurement error using the procedure described in [85, 87] (see Appendix B). From the linear Gaussian model, it appears that for the time-step used here, the measurement error is overestimated. Besides, estimated measurement error for individual cells may not be reliable. Thus, we take an informal approach and compare the population-averaged estimate of the contribution of measurement error to the population-averaged estimate of the quantity in question.

The statistically and quantitatively significant non-Gaussian effects are tabulated in Table 4. No chirality was detected. First, we note that the existence of non-Gaussian effects depends on the choice of coordinate. This is particularly relevant in our situation, where although we defined our shape variables based on linearization about a spherical shape, in the regime of actual shapes obtained the mapping from the deformation coefficients defining the distance function $r(\theta, \phi)$ to our shape variables is highly nonlinear (see Appendix C). We have attempted to roughly estimate the contribution of this nonlinearity to the non-Gaussian coefficients, assuming linear Gaussian dynamics for the deformation coefficients, orientational dynamics, and center-of-mass motion. These are listed in the “Est.” columns in Table 4, expressed as a fraction of the measured value. We see that for most quantities involving shape alone, there is a significant possibility of non-Gaussian effects being explained by the nonlinear shape mapping. However, for the quantities involving orientational dynamics or center-of-mass motion, the estimated contribution is small and thus we think it is likely not due to the nonlinearity of shape coordinates. Thus, we focus our attention on these quantities.

First, we have $\Re \langle \Delta s_2^0 \dot{s}_2^1 \dot{\theta} e^{-i\phi} \rangle, \Re \langle \Delta s_2^0 d[\dot{s}_2^1, \dot{\theta} e^{-i\phi}] / dt \rangle < 0$. This expresses a negative correlation between elongation and joint fluctuations of \dot{s}_2^1 and $\dot{\theta} e^{i\phi}$. This makes sense as a more elongated shape will be less affected by fluctuations of direction at the front. Next, we have quantities of the opposite

⁵It is shown in [85] how to extract terms in the Langevin equation from trajectories. However, the time-step is too large relative to dynamics to justify a discrete-time approach, and it would be extremely troublesome to relate discrete-time measurements to continuous-time parameters. Thus, we opted not to do this at all.

TABLE 4. Statistically and quantitatively significant non-Gaussian effects.

Quantity and sign	Adj. p -value	Est.	Quantity and sign	Adj. p -value	Est.
$\Re\langle s_2^1 s_2^0 s_2^{2*} \rangle > 0$	0.019	0.70	$\Re\langle s_2^1 \dot{\theta} e^{i\phi} s_2^{2*} \rangle < 0$	7.8×10^{-5}	0.18
$\Re\langle s_2^1 s_3^1 s_3^{2*} \rangle > 0$	7.5×10^{-4}	0.60	$\Re\langle s_2^1 \dot{\theta} e^{i\phi} s_3^{2*} \rangle < 0$	0.024	-0.26
$\Re\langle s_3^1 s_3^0 s_2^{2*} \rangle > 0$	7.5×10^{-4}	0.37	$\Re\langle s_2^1 v^1 s_2^{2*} \rangle < 0$	2.9×10^{-3}	0.08
$\Re\langle \Delta s_2^0 s_2^1 \dot{\theta} e^{-i\phi} \rangle < 0$	0.029	0.01	$\Re\langle s_3^1 \dot{\theta} e^{i\phi} s_3^{2*} \rangle < 0$	4.0×10^{-4}	0.08
$\Re\langle \Delta s_3^0 s_3^1 \dot{\theta} e^{-i\phi} \rangle < 0$	0.031	0.05	$\Re\langle \Delta s_2^0 d[s_2^1, \dot{\theta} e^{-i\phi}]/dt \rangle < 0$	2.1×10^{-3}	0.01
$\Re\langle s_2^1 s_2^0 \dot{\theta} e^{-i\phi} \rangle > 0$	2.8×10^{-4}	-0.07	$\Re\langle s_2^1 d[s_2^0, \dot{\theta} e^{-i\phi}]/dt \rangle > 0$	8.8×10^{-4}	-0.04
$\Re\langle s_2^1 s_2^0 v^{1*} \rangle > 0$	5.0×10^{-3}	-0.02	$\Re\langle s_2^1 d[s_2^0, v^{1*}]/dt \rangle > 0$	6.4×10^{-3}	0.01
$\Re\langle s_3^1 s_2^0 \dot{\theta} e^{-i\phi} \rangle > 0$	0.016	0.12	$\Re\langle s_2^2 d[s_2^0, s_2^{2*}]/dt \rangle < 0$	0.047	0.69
$\Re\langle s_3^1 s_2^0 v^{1*} \rangle > 0$	0.017	0.06	$\Re\langle s_2^2 d[s_3^0, s_3^{2*}]/dt \rangle < 0$	1.1×10^{-3}	0.97
$\Re\langle s_2^2 s_2^0 s_2^{2*} \rangle < 0$	0.025	0.94	$\Re\langle s_3^2 d[s_2^0, s_2^{2*}]/dt \rangle < 0$	0.022	0.89
$\Re\langle s_2^2 s_3^0 s_3^{2*} \rangle < 0$	2.9×10^{-3}	1.42	$\Re\langle s_3^2 d[s_3^0, s_2^{2*}]/dt \rangle < 0$	0.024	0.43
$\Re\langle s_2^{2*} s_2^1 v^1 \rangle > 0$	4.0×10^{-4}	-0.08	$\Re\langle s_2^{2*} d[s_3^1, s_3^1]/dt \rangle > 0$	4.0×10^{-3}	0.69
$\Re\langle s_2^{2*} s_3^1 s_3^1 \rangle > 0$	3.0×10^{-3}	1.04	$\Re\langle s_2^1 d[s_2^1, s_2^{2*}]/dt \rangle > 0$	0.017	1.10
$\Re\langle s_3^{2*} s_2^1 s_3^1 \rangle > 0$	0.012	-0.15	$\Re\langle s_2^1 d[\dot{\theta} e^{i\phi}, s_2^{2*}]/dt \rangle < 0$	9.3×10^{-3}	0.13
$\Re\langle s_3^{2*} s_2^1 \dot{\theta} e^{i\phi} \rangle > 0$	2.0×10^{-3}	-0.15	$\Re\langle s_3^1 d[s_2^1, s_3^{2*}]/dt \rangle > 0$	2.0×10^{-4}	0.31
$\Re\langle s_3^{2*} s_2^1 v^1 \rangle > 0$	2.7×10^{-5}	-0.01	$\Re\langle (\dot{\theta} e^{i\phi})^2 s_2^{2*} \rangle < 0$	0.011	0.20
$\Re\langle s_2^1 s_2^1 s_2^{2*} \rangle > 0$	0.021	1.21	$\Re L(v^1 s_2^{2*}, s_3^1) > 0$	0.038	-0.04
$\Re\langle s_2^1 s_3^1 s_3^{2*} \rangle > 0$	6.6×10^{-4}	0.64			

sign: $\Re\langle s_2^1 s_2^0 \dot{\theta} e^{-i\phi} \rangle, \Re\langle s_2^1 d[s_2^0, \dot{\theta} e^{-i\phi}]/dt \rangle, \Re\langle s_2^1 s_2^0 v^{1*} \rangle, \Re\langle s_2^1 d[s_2^0, v^{1*}]/dt \rangle, \Re\langle s_3^1 s_2^0 \dot{\theta} e^{-i\phi} \rangle, \Re\langle s_3^1 s_2^0 v^{1*} \rangle > 0$. These also make sense as a non-straight cell will change direction more if it elongates faster. It is notable that in the case of a martingale in Markovian dynamics, opposite signs are required for vanishing of the third-order angular momentum [87]. This can be intuitively understood as follows. Suppose we start with a low s_2^0 with $s_2^1 = 0$; we then have strongly correlated fluctuations of s_2^1 and $\dot{\theta} e^{i\phi}$. Now, we have a value of s_2^1 positively correlated with the fluctuation of $\dot{\theta} e^{i\phi}$. If $\dot{\theta} e^{i\phi}$ were to continue in the same direction, this would imply an increase in s_2^0 , meaning an effect in the opposite direction as the low s_2^0 we started with. However, it is possible that there are angular momenta which are actually quantitatively significant but that we do not have the necessary statistics to resolve them.

Next, we have $\Re\langle \Delta s_3^0 s_2^1 \dot{\theta} e^{-i\phi} \rangle < 0$. Recalling that a widening of the front is a more negative s_3^0 , this corresponds to a positive correlation between a wider front and joint fluctuations of s_2^1 and $\dot{\theta} e^{i\phi}$.

Next, we have another pair of sets of quantities with opposite sign: $\Re\langle s_2^{2*} s_2^1 v^1 \rangle, \Re\langle s_3^{2*} s_2^1 \dot{\theta} e^{i\phi} \rangle, \Re\langle s_3^{2*} s_2^1 v^1 \rangle > 0$, whereas $\Re\langle s_2^1 \dot{\theta} e^{i\phi} s_2^{2*} \rangle, \Re\langle s_2^1 \dot{\theta} e^{i\phi} s_3^{2*} \rangle, \Re\langle s_2^1 v^1 s_2^{2*} \rangle, \Re\langle s_3^1 \dot{\theta} e^{i\phi} s_3^{2*} \rangle, \Re\langle s_2^1 d[\dot{\theta} e^{i\phi}, s_2^{2*}]/dt \rangle < 0$. The first

set of quantities says that joint fluctuations of shape and direction tend to occur along lateral elongation of the front of the cell. The second set of quantities is somewhat less intuitive, but can be understood as follows. If an $m = 1$ cell deformation mode and the cell's direction of motion or change in orientation are aligned, then the front widens laterally perpendicular to the deformation mode. If they are anti-aligned, then the front widens laterally parallel to the deformation mode. Again, as in the previous case, the quantities of opposite signs make opposite contributions to the third-order angular momentum.

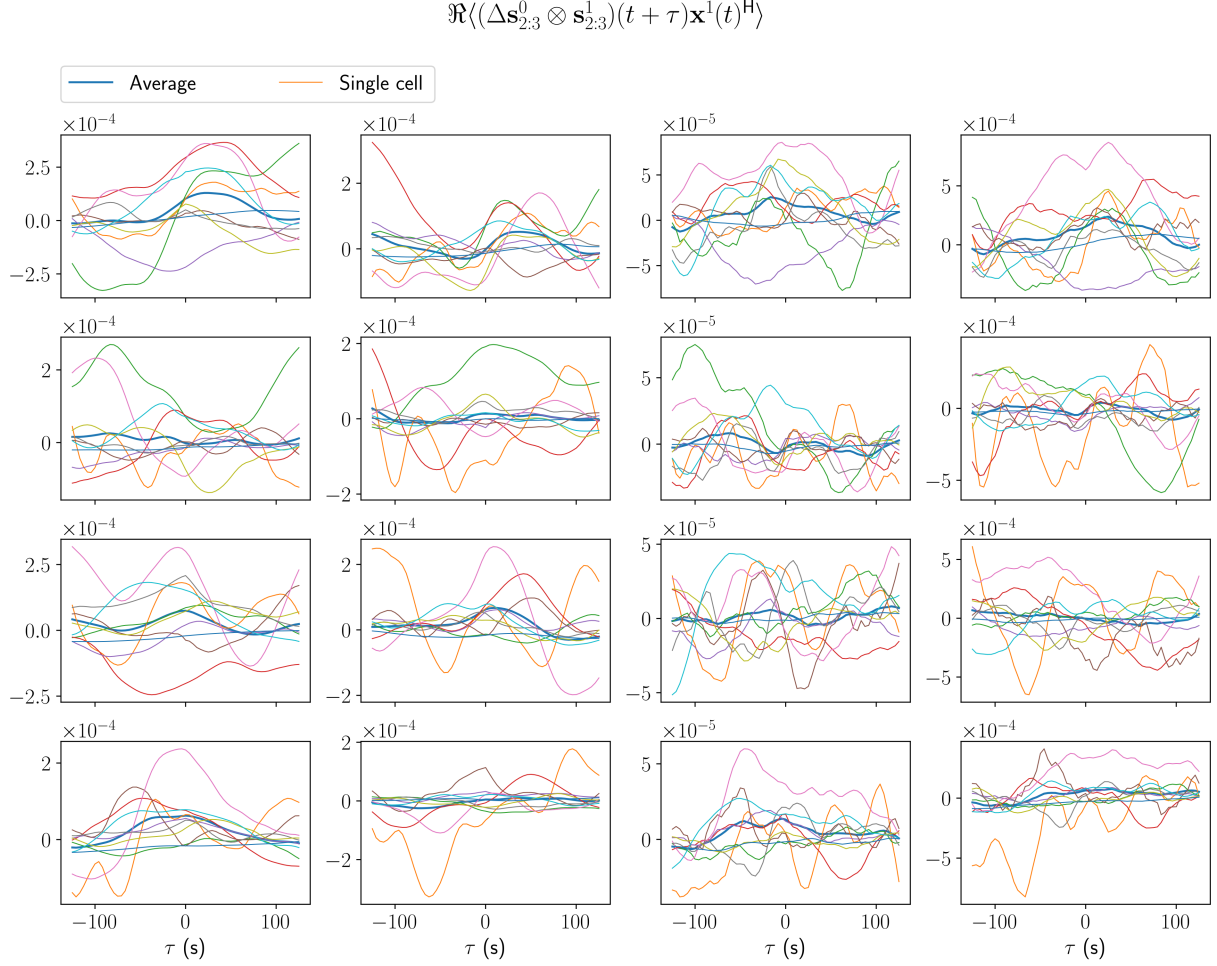
Lastly, we have the two quantities from the second group of the partition mentioned at the beginning of this section. The first quantity, $\Re((\dot{\theta}e^{i\phi})^2 \dot{s}_2^{2*}) < 0$, is time-antisymmetric and can be interpreted as a negative correlation between \dot{s}_2^2 and orientational changes. The second quantity, $\Re L(v^1 \dot{s}_2^{2*}, \dot{s}_3^1) > 0$, is time-symmetric and can be interpreted as a positive correlation between the acceleration \ddot{s}_3^1 and $v^1 \dot{s}_2^{2*}$, which is admittedly difficult to intuit.

Ideally, the next step would be to investigate the third-order covariance functions and evaluate if they are consistent with a description based on an underdamped Langevin equation. However, given that there are hundreds of coefficients, such an evaluation would be difficult mathematically as well as visually with a sample size as small as ours. Already with equal-time quantities, we are having difficulties with the small p -values required. Nevertheless, we have included some third-order covariance functions for illustration (Figs. 5 and 6).

6. CONCLUSIONS

We have elucidated the ‘‘laws of motion’’ obeyed by T cell morphodynamics and migration in 3D collagen matrices. We have corrected previous understanding which incorrectly posited discrete structure of the probability distribution of dynamics and periodic oscillations of shape. We have introduced a new method of 3D shape description relative to the polarization axis, preserving different possible modes of shape variation, and have described dynamics using an underdamped Langevin equation. This approach reveals different correlation times for different modes: the $m = 0$ modes have correlation times approximately 60 s, the $(l, m) = (2, 1)$ and $(l, m) = (2, 2)$ modes approximately 90 s, and the $(l, m) = (3, 1)$ and $(l, m) = (3, 2)$ modes approximately 30 s. In addition, we have quantified time-irreversibility, which has been qualitatively observed in previous studies. Furthermore, we have extracted novel coefficients describing non-Gaussianity and have found patterns in the signs of the coefficients. Also, we did not find statistically significant correlations between phase-space velocities and quadratic polynomials of shape. However, our analysis is limited by small sample size. Still, we have been able to determine the presence of some non-Gaussian effects by taking into account possible population heterogeneity when calculating statistics.

While mechanistic insights likely cannot be gleaned at this stage, we have characterized biology at the level of emergent behavior, which is an important step in understanding a complex system such as cell migration. Future work could involve analyzing larger datasets and comparing different biological conditions. In particular, multiple biological replicates would be desired to confirm the findings. Additionally, temporal and population variability could be quantified. In this work, we only considered temporally- and population-averaged dynamics. The role of temporal and population variability in cell migration has been considered in [60, 62, 90, 91]. Augmenting our analysis to include these aspects would form the basis for a data-driven understanding of 3D cell migration, an area where there is currently limited research.


 FIGURE 5. Third-order covariance functions. Velocities are in units of $\mu\text{m}/\text{fr}$.

7. APPENDIX A

In this appendix, we describe the procedure for converting discrete-time to continuous-time, and give the values of the parameters of the linear Gaussian model. We write the linear Gaussian underdamped Langevin equation as:

$$(12) \quad \begin{pmatrix} \dot{\mathbf{x}} \\ \dot{\mathbf{\dot{x}}} \end{pmatrix} = \mathbf{\Gamma} \begin{pmatrix} \mathbf{x} \\ \dot{\mathbf{x}} \end{pmatrix} + \begin{pmatrix} \mathbf{0} \\ \boldsymbol{\xi} \end{pmatrix}, \quad \langle \boldsymbol{\xi}(t)\boldsymbol{\xi}(t')^T \rangle = 2\mathbf{D}\delta(t - t')$$

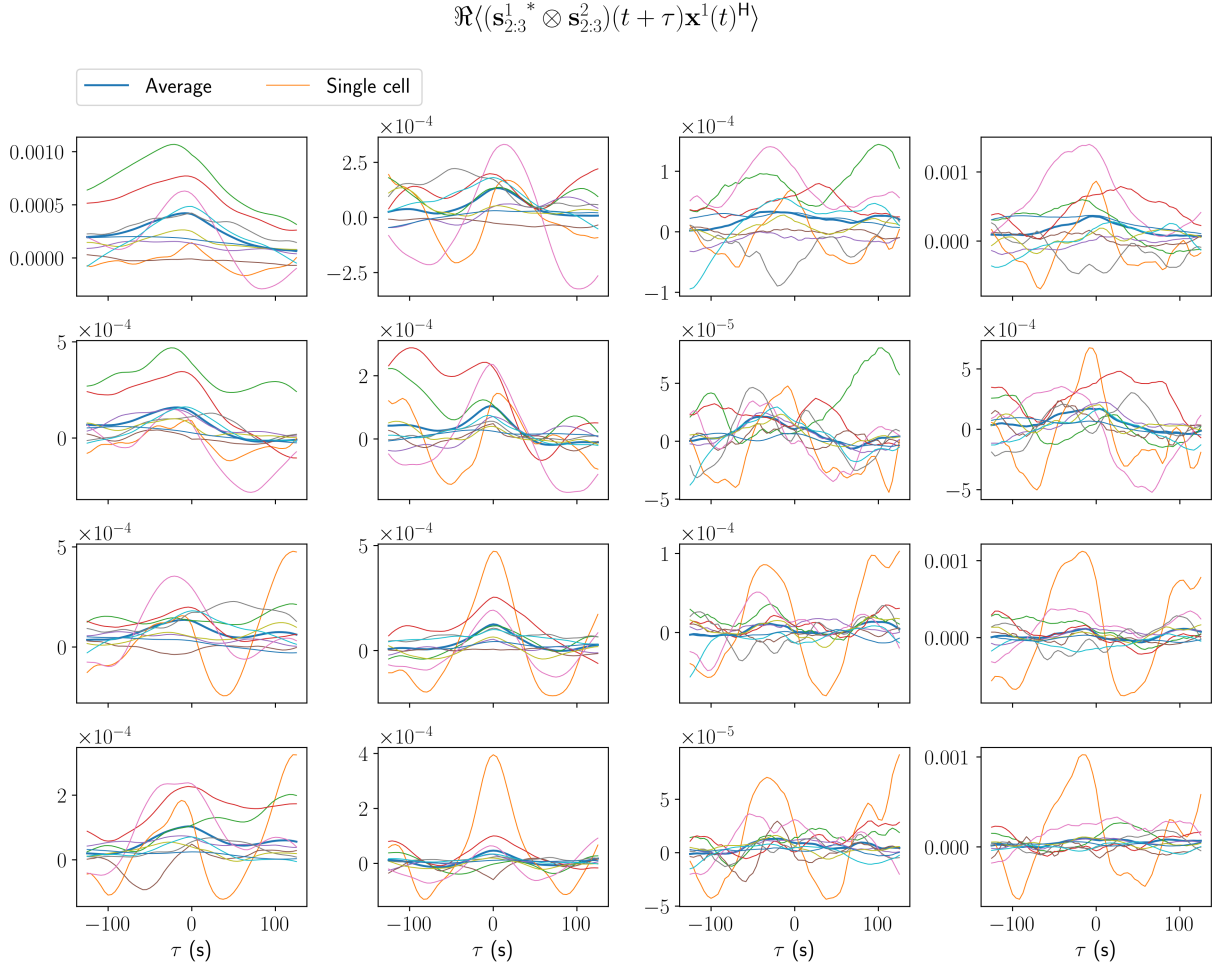


FIGURE 6. Third-order covariance functions. Velocities are in units of $\mu\text{m}/\text{fr}$.

(using Hermitian conjugate as appropriate for complex variables). We introduce the covariance matrix:

$$(13) \quad \mathbf{C} := \begin{pmatrix} \langle \mathbf{x}\mathbf{x}^T \rangle & \langle \mathbf{x}\dot{\mathbf{x}}^T \rangle \\ \langle \dot{\mathbf{x}}\mathbf{x}^T \rangle & \langle \dot{\mathbf{x}}\dot{\mathbf{x}}^T \rangle \end{pmatrix},$$

which can be determined from $\mathbf{\Gamma}$ and \mathbf{D} using the Lyapunov equation [87]. We have:

$$(14) \quad \int_0^\tau dt \langle \dot{x}^i(t) x^j(0) \rangle = [\mathbf{\Gamma}^{-1}(e^{\mathbf{\Gamma}\tau} - \mathbf{1})\mathbf{C}]^{\dot{x}^i x^j},$$

$$(15) \quad \int_0^\tau dt \langle x^i(t) \dot{x}^j(0) \rangle = [\mathbf{\Gamma}^{-1}(e^{\mathbf{\Gamma}\tau} - \mathbf{1})\mathbf{C}]^{x^i \dot{x}^j},$$

$$(16) \quad \int_0^\tau dt \int_0^\tau dt' \langle \dot{x}^i(t) \dot{x}^j(t') \rangle = [\mathbf{\Gamma}^{-2}(e^{\mathbf{\Gamma}\tau} - \mathbf{1} - \mathbf{\Gamma}\tau)\mathbf{C}]^{\dot{x}^i \dot{x}^j} + [\mathbf{\Gamma}^{-2}(e^{\mathbf{\Gamma}\tau} - \mathbf{1} - \mathbf{\Gamma}\tau)\mathbf{C}]^{\dot{x}^j \dot{x}^i},$$

$$(17) \quad \int_{n\tau}^{(n+1)\tau} dt \int_0^\tau dt' \langle \dot{x}^i(t) \dot{x}^j(t') \rangle = [\mathbf{\Gamma}^{-2}(e^{\mathbf{\Gamma}\tau} + e^{-\mathbf{\Gamma}\tau} - 2\mathbf{1})e^{n\mathbf{\Gamma}\tau}\mathbf{C}]^{\dot{x}^i \dot{x}^j}, \quad n \geq 1,$$

where $\mathbf{1}$ is the identity matrix.

For $m = 0$, we have for the linear Gaussian model:

$$(18) \quad \mathbf{C}^0 = \begin{pmatrix} 3.9 \times 10^{-3} & -5.2 \times 10^{-4} & 0 & -1.4 \times 10^{-4} & 3.1 \times 10^{-3} \\ -5.2 \times 10^{-4} & 2.2 \times 10^{-3} & 1.4 \times 10^{-4} & 0 & -1.2 \times 10^{-3} \\ 0 & 1.4 \times 10^{-4} & 1.8 \times 10^{-4} & -1.2 \times 10^{-5} & -6.4 \times 10^{-4} \\ -1.4 \times 10^{-4} & 0 & -1.2 \times 10^{-5} & 1.2 \times 10^{-4} & -3.3 \times 10^{-5} \\ 3.1 \times 10^{-3} & -1.2 \times 10^{-3} & -6.4 \times 10^{-3} & -3.3 \times 10^{-5} & 0.048 \end{pmatrix}$$

$$(19) \quad \mathbf{A}_{\mathbf{x}}^0 = \begin{pmatrix} -0.026 & 0.025 \\ -0.022 & -0.060 \\ 0.41 & -0.25 \end{pmatrix}$$

$$(20) \quad \mathbf{A}_{\mathbf{v}}^0 = \begin{pmatrix} -0.51 & 0.26 & -9.6 \times 10^{-3} \\ -0.05 & -0.62 & -6.3 \times 10^{-3} \\ 0.7 & -4.8 & -0.56 \end{pmatrix}$$

$$(21) \quad \mathbf{D}^0 = \begin{pmatrix} 8.5 \times 10^{-5} & -1.7 \times 10^{-5} & -1.2 \times 10^{-4} \\ -1.7 \times 10^{-5} & 7.1 \times 10^{-5} & 4.4 \times 10^{-4} \\ -1.2 \times 10^{-4} & 4.4 \times 10^{-4} & 2.6 \times 10^{-2} \end{pmatrix},$$

where time is measured in units of frames and velocities are measured in $\mu\text{m}/\text{fr}$. We have the eigendecomposition:

$$(22) \quad \mathbf{\Gamma}^0 = (\mathbf{S}^0) \text{diag}(-0.083, -0.21 + 0.10i, c.c., -0.46, -0.72)(\mathbf{S}^0)^{-1}$$

$$(23) \quad \mathbf{S}^0 = \begin{pmatrix} -0.59 & -0.38 - 0.07i & c.c. & 0.90 & -0.01 \\ 0.78 & -0.18 - 0.17i & c.c. & -0.05 & -0.05 \\ 0.049 & 0.087 - 0.022i & c.c. & -0.42 & 0.007 \\ -0.064 & 0.054 + 0.018i & c.c. & 0.022 & 0.035 \\ -0.19 & -0.88 & c.c. & -0.13 & 1.00 \end{pmatrix},$$

where c.c. denotes complex conjugate of the previous column. For $m = 1$, we have:

$$(24) \quad \mathbf{C}^1 = \begin{pmatrix} 8.3 \times 10^{-3} & 9.9 \times 10^{-4} & 0 & -1.8 \times 10^{-4} & 1.2 \times 10^{-3} & 9.3 \times 10^{-3} \\ 9.9 \times 10^{-4} & 3.0 \times 10^{-3} & 1.8 \times 10^{-4} & 0 & -1.8 \times 10^{-4} & 9.8 \times 10^{-4} \\ 0 & 1.8 \times 10^{-4} & 2.7 \times 10^{-4} & -3.5 \times 10^{-5} & -2.2 \times 10^{-4} & -4.9 \times 10^{-4} \\ -1.8 \times 10^{-4} & 0 & -3.5 \times 10^{-5} & 2.8 \times 10^{-4} & 2.3 \times 10^{-4} & 7.0 \times 10^{-4} \\ 1.2 \times 10^{-3} & -1.8 \times 10^{-4} & -2.2 \times 10^{-4} & 2.3 \times 10^{-4} & 1.6 \times 10^{-3} & 6.8 \times 10^{-3} \\ 9.3 \times 10^{-3} & 9.8 \times 10^{-4} & -4.9 \times 10^{-4} & 7.0 \times 10^{-4} & 6.8 \times 10^{-3} & 0.087 \end{pmatrix}$$

$$(25) \quad \mathbf{A}_{\mathbf{x}}^1 = \begin{pmatrix} -0.070 & 0.105 \\ 0.039 & -0.143 \\ 0.18 & -0.28 \\ 1.13 & -0.97 \end{pmatrix}$$

$$(26) \quad \mathbf{A}_{\mathbf{v}}^1 = \begin{pmatrix} -1.33 & 0.85 & -1.9 \times 10^{-3} & 0.040 \\ 0.71 & -1.19 & -0.048 & -0.033 \\ 1.7 & -1.6 & -0.81 & -0.034 \\ 14 & -11 & 1.4 & -1.3 \end{pmatrix}$$

$$(27) \quad \mathbf{D}^1 = \begin{pmatrix} 3.9 \times 10^{-4} & -2.8 \times 10^{-4} & -6.6 \times 10^{-4} & -4.2 \times 10^{-3} \\ -2.8 \times 10^{-4} & 3.9 \times 10^{-4} & 7.0 \times 10^{-4} & 4.2 \times 10^{-3} \\ -6.6 \times 10^{-4} & 7.0 \times 10^{-4} & 2.0 \times 10^{-3} & 9.7 \times 10^{-3} \\ -4.2 \times 10^{-3} & 4.2 \times 10^{-3} & 9.7 \times 10^{-3} & 0.104 \end{pmatrix}$$

$$(28) \quad \mathbf{\Gamma}^1 = (\mathbf{S}^1) \text{diag}(-0.049, -0.15, -0.35, -0.44, -0.99, -2.60)(\mathbf{S}^1)^{-1}$$

$$(29) \quad \mathbf{S}^1 = \begin{pmatrix} 0.78 & -0.042 & -0.37 & -0.21 & -0.026 & 0.021 \\ -0.25 & -0.87 & -0.65 & -0.10 & 0.022 & -0.044 \\ -0.039 & 0.007 & 0.13 & 0.091 & 0.067 & -0.020 \\ 0.012 & 0.13 & 0.22 & 0.046 & -0.058 & 0.044 \\ 0.14 & 0.080 & -0.001 & 0.12 & -0.13 & 0.32 \\ 0.55 & -0.46 & -0.61 & 0.96 & -0.99 & -0.95 \end{pmatrix}.$$

For $m = 2$, we have:

$$(30) \quad \mathbf{C}^2 = \begin{pmatrix} 5.3 \times 10^{-3} & 2.1 \times 10^{-3} & 0 & -8.4 \times 10^{-5} \\ 2.1 \times 10^{-3} & 2.0 \times 10^{-3} & 8.4 \times 10^{-5} & 0 \\ 0 & 8.4 \times 10^{-5} & 1.1 \times 10^{-4} & 5.7 \times 10^{-5} \\ -8.4 \times 10^{-5} & 0 & 5.7 \times 10^{-5} & 1.1 \times 10^{-4} \end{pmatrix}$$

$$(31) \quad \mathbf{A}_{\mathbf{x}}^2 = \begin{pmatrix} -0.029 & 0.030 \\ 0.006 & -0.062 \end{pmatrix}$$

$$(32) \quad \mathbf{A}_{\mathbf{v}}^2 = \begin{pmatrix} -0.67 & 0.24 \\ -0.01 & -0.50 \end{pmatrix}$$

$$(33) \quad \mathbf{D}^2 = \begin{pmatrix} 5.8 \times 10^{-5} & 2.2 \times 10^{-5} \\ 2.2 \times 10^{-5} & 5.5 \times 10^{-5} \end{pmatrix}$$

$$(34) \quad \mathbf{\Gamma}^2 = (\mathbf{S}^2) \text{diag}(-0.042, -0.20, -0.31, -0.61)(\mathbf{S}^2)^{-1}$$

$$(35) \quad \mathbf{S}^2 = \begin{pmatrix} 0.99 & -0.27 & 0.46 & 0.85 \\ 0.14 & -0.94 & 0.84 & 0.06 \\ -0.042 & 0.055 & -0.14 & -0.52 \\ -0.006 & 0.19 & -0.26 & -0.036 \end{pmatrix}.$$

8. APPENDIX B

In this appendix, we calculate the contribution of measurement error to the estimation of $L(\dot{x}^i \dot{x}^j, \dot{x}^k)$. Let $\mathbf{y} := \mathbf{x} + \boldsymbol{\eta}$ denote the measured values, with $\boldsymbol{\eta}$ the measurement error. We only consider second moments of $\boldsymbol{\eta}$, denoted by $\mathbf{\Lambda}$, and may be state-dependent. Following [85], we make the assumption $\mathbf{\Lambda} \ll \langle \dot{\mathbf{x}} \dot{\mathbf{x}}^\top \rangle (\Delta t)^2$, where Δt is the time-step, necessary for validity of the estimation procedure. We have verified that this is the case for our dataset. We define $\tilde{\mathbf{\Lambda}} := \mathbf{\Lambda} (\Delta t)^{-2}$ so that $\tilde{\mathbf{\Lambda}} = \mathcal{O}((\Delta t)^0)$. The estimate is given by:

$$(36) \quad L(\dot{x}^i \dot{x}^j, \dot{x}^k) \approx (\Delta t)^{-4} \langle (y^i(t + \Delta t) - y^i(t))(y^j(t + \Delta t) - y^j(t))(y^k(t + 2\Delta t) - y^k(t + \Delta t)) \\ - (y^i(t + 2\Delta t) - y^i(t + \Delta t))(y^j(t + 2\Delta t) - y^j(t + \Delta t))(y^k(t + \Delta t) - y^k(t)) \rangle.$$

The contribution of measurement error is seen to be:

$$(37) \quad (\Delta t)^{-2} \langle (\tilde{\mathbf{\Lambda}}^{ij}(t + \Delta t) + \tilde{\mathbf{\Lambda}}^{ij}(t))(x^k(t + 2\Delta t) - x^k(t + \Delta t)) \\ - (\tilde{\mathbf{\Lambda}}^{jj}(t + 2\Delta t) + \tilde{\mathbf{\Lambda}}^{jj}(t + \Delta t))(x^k(t + \Delta t) - x^k(t)) \\ - \tilde{\mathbf{\Lambda}}^{ik}(t + \Delta t)(x^j(t + \Delta t) - x^j(t)) - \tilde{\mathbf{\Lambda}}^{jk}(t + \Delta t)(x^i(t + \Delta t) - x^i(t)) \\ + \tilde{\mathbf{\Lambda}}^{ik}(t + \Delta t)(x^j(t + 2\Delta t) - x^j(t + \Delta t)) + \tilde{\mathbf{\Lambda}}^{jk}(t + \Delta t)(x^i(t + 2\Delta t) - x^i(t + \Delta t)) \rangle.$$

Now, we have:

$$(38) \quad (\Delta t)^{-2} \langle \tilde{\mathbf{\Lambda}}^{ij}(t + \Delta t)(x^k(t + 2\Delta t) - 2x^k(t + \Delta t) + x^k(t)) \rangle = \langle \tilde{\mathbf{\Lambda}}^{ij} \circ \ddot{x}^k \rangle + \mathcal{O}(\Delta t),$$

where \circ denotes Stratonovich convention. The last two lines of Eq. (37) therefore contribute:

$$(39) \quad \langle \tilde{\mathbf{\Lambda}}^{ik} \circ \ddot{x}^j \rangle + \langle \tilde{\mathbf{\Lambda}}^{jk} \circ \ddot{x}^i \rangle + \mathcal{O}(\Delta t).$$

TABLE 5. Correction factors and offsets associated with nonlinear shape map.

γ_2^0	δ_2	γ_3^0	δ_3	γ_2^1	γ_3^1	γ_2^2	γ_3^2	γ_3^3
1.33	-0.023	3.05	0.083	1.55	1.95	2.04	0.54	2.53

The remaining terms can be written:

$$(40) \quad (\Delta t)^{-2} \langle (\tilde{\Lambda}^{ij}(t) + \tilde{\Lambda}^{ij}(t + 2\Delta t))(x^k(t + 2\Delta t) - 2x^k(t + \Delta t) + x^k(t)) \\ + \tilde{\Lambda}^{ij}(t)(x^k(t + \Delta t) - x^k(t)) - \tilde{\Lambda}^{ij}(t + 2\Delta t)(x^k(t + 2\Delta t) - x^k(t + \Delta t)) \rangle.$$

The second line of Eq. (40) evaluates to $\langle \tilde{\Lambda}^{ij} \circ \ddot{x}^k \rangle + \mathcal{O}(\Delta t)$. The first line of Eq. (40) can be evaluated by using an Itô–Taylor expansion [85], resulting in:

$$(41) \quad (\Delta t)^{-2} \langle (\tilde{\Lambda}^{ij}(t) + \tilde{\Lambda}^{ij}(t + 2\Delta t))(x^k(t + 2\Delta t) - 2x^k(t + \Delta t) + x^k(t)) \rangle = 2\langle \tilde{\Lambda}^{ij} \circ \ddot{x}^k \rangle + \mathcal{O}(\Delta t).$$

The final result is therefore:

$$(42) \quad \langle 4\tilde{\Lambda}^{ij} \circ \ddot{x}^k + \tilde{\Lambda}^{ik} \circ \ddot{x}^j + \tilde{\Lambda}^{jk} \circ \ddot{x}^i \rangle + \mathcal{O}(\Delta t).$$

Finally, we need to estimate $\langle \tilde{\Lambda}^{ij} \circ \ddot{x}^k \rangle$ from time-lapse data. However, we cannot do this by using the estimator for Λ described in [85, 87] together with the direct estimator for \ddot{x}^k , because this will introduce terms involving Λ^{ik} and Λ^{jk} . Instead, we need to infer $\langle \circ \ddot{\mathbf{x}} \mid \mathbf{x}, \dot{\mathbf{x}} \rangle$ and plug in the obtained function of \mathbf{x} and $\dot{\mathbf{x}}$.

9. APPENDIX C

In this appendix, we describe the estimation of contributions of the shape mapping to non-Gaussian effects. We consider a distance function:

$$(43) \quad r(\theta, \phi) = 1 + \sum_{l=2}^3 \sum_{m=-l}^l r_l^m Y_l^m(\theta, \phi)$$

(in actuality, we use real spherical harmonics) and investigate the map $r_l^m \mapsto s_l^m$. First, we attempted to solve for each s_l^m the corresponding r_l^m . However, in many cases the obtained solutions had large negative values of $r(\theta, \phi)$ and were thus unreliable. Therefore, we took another approach. We then tried to estimate the distribution of r_l^m by generating for each cell a Gaussian distribution with the same mean and variance as s_l^m , and setting the r_l^m values to these multiplied by some factor γ_l^m and for $m = 0$ adding an offset δ_l , to be determined by equating the resulting mean and variance of the corresponding s_l^m for $m = 0$ and the resulting variance for $m > 0$. The calculated factors γ_l^m and offsets δ_l are tabulated in Table 5. The resulting $r(\theta, \phi)$ often had negative minimum values, but these were generally small compared to the maximum values (Fig. 7), especially when raised to a power (after taking centroid offset into account) and when combined with the fact that larger r values take up more surface area, so we deemed this to be acceptable. The statistics for the calculated s_l^m for the entire population are $\text{Var}(s_2^0) = 0.014$, $\text{Var}(s_3^0) = 4.6 \times 10^{-3}$ (fitted), and $\text{Cov}(s_2^0, s_3^0) = -2.7 \times 10^{-3}$, compared to a true value of -4.0×10^{-3} . The cell-wise statistics are $\text{Var}(s_2^0) = 4.5 \times 10^{-3}$, $\text{Var}(s_3^0) = 3.3 \times 10^{-3}$, $\text{Cov}(s_2^0, s_3^0) = -0.5 \times 10^{-3}$, $\Re\langle s_2^1 s_3^{1*} \rangle = 0.6 \times 10^{-3}$, and $\Re\langle s_2^2 s_3^{2*} \rangle = 2.7 \times 10^{-3}$ (compare with Table 1).

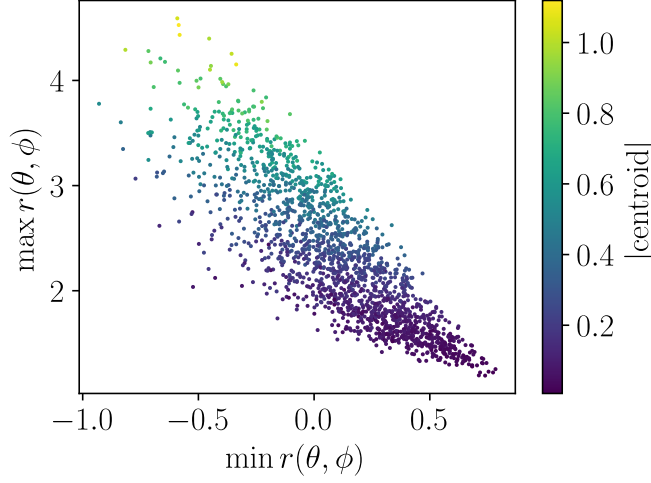


FIGURE 7. Minimum and maximum $r(\theta, \phi)$, along with distance from origin to centroid, for simulated data.

Next, we fit the obtained s_i^m to quadratic polynomials in r_i^m . Along with azimuthal and chiral symmetry, the shape map obeys the symmetry of flipping the z -axis. In addition, a spherical shape must have $s_i^m = 0$. This leads to:

(44)

$$s_2^0 \approx \alpha_2^0 r_2^0 + \beta_{22}^{00} (r_2^0)^2 + \beta_{33}^{00} (r_3^0)^2 + \beta_{22}^{11*} r_2^1 r_2^{1*} + \beta_{33}^{11*} r_3^1 r_3^{1*} + \beta_{22}^{22*} r_2^2 r_2^{2*} + \beta_{33}^{22*} r_3^2 r_3^{2*} + \beta_{33}^{33*} r_3^3 r_3^{3*},$$

(45)

$$s_3^0 \approx \alpha_3^0 r_3^0 + \beta_{23}^{00} r_2^0 r_3^0 + \beta_{23}^{11*} \Re[r_2^1 r_3^{1*}] + \beta_{23}^{22*} \Re[r_2^2 r_3^{2*}],$$

(46)

$$s_2^1 \approx \alpha_2^1 r_2^1 + \beta_{22}^{01} r_2^0 r_2^1 + \beta_{33}^{01} r_3^0 r_3^1 + \beta_{22}^{1*2} r_2^1 r_2^2 + \beta_{33}^{1*2} r_3^1 r_3^2 + \beta_{33}^{2*3} r_3^2 r_3^3,$$

(47)

$$s_3^1 \approx \alpha_3^1 r_3^1 + \beta_{23}^{01} r_2^0 r_3^1 + \beta_{32}^{01} r_3^0 r_2^1 + \beta_{23}^{1*2} r_2^1 r_3^2 + \beta_{32}^{1*2} r_3^1 r_2^2 + \beta_{23}^{2*3} r_2^2 r_3^3,$$

(48)

$$s_2^2 \approx \alpha_2^2 r_2^2 + \beta_{22}^{02} r_2^0 r_2^2 + \beta_{33}^{02} r_3^0 r_3^2 + \beta_{22}^{11} (r_2^1)^2 + \beta_{33}^{11} (r_3^1)^2 + \beta_{33}^{1*3} r_3^1 r_3^3,$$

(49)

$$s_3^2 \approx \alpha_3^2 r_3^2 + \beta_{23}^{02} r_2^0 r_3^2 + \beta_{32}^{02} r_3^0 r_2^2 + \beta_{23}^{11} r_2^1 r_3^1 + \beta_{23}^{1*3} r_2^1 r_3^3,$$

(50)

$$s_3^3 \approx \alpha_3^3 r_3^3 + \beta_{23}^{03} r_2^0 r_3^3 + \beta_{23}^{12} r_2^1 r_3^2 + \beta_{32}^{12} r_3^1 r_2^2.$$

The coefficients of the fit, along with the root mean squared magnitude of the regressors, are given in Table 6, in the order written in Eqs. (44)–(50). Despite high R^2 values ($\gtrsim 0.9$), the fitted coefficients changed when the distribution of r_i^m was modified (not shown), indicating a lack of predictive power and nonlinearity beyond quadratic.

TABLE 6. Coefficients of a quadratic fit for the shape mapping.

	α	β
	RMS of regressors	
s_2^0	1.02	-0.73, 0.08, 0.18, 0.28, -0.38, -0.83, -0.34
	0.247	0.092, 0.178, 0.031, 0.022, 0.039, 0.001, 0.009
s_3^0	0.56	-0.74, -0.18, -1.92
	0.342	0.106, 0.014, 0.005
s_2^1	0.66	-0.05, 0.23, 0.79, 0.50, 2.54
	0.140	0.034, 0.044, 0.023, 0.003, 0.002
s_3^1	0.53	-0.41, 0.05, 0.77, 0.65, -0.49
	0.117	0.030, 0.049, 0.004, 0.019, 0.012
s_2^2	0.66	-1.14, 0.07, 0.27, 0.18, -0.23
	0.159	0.035, 0.010, 0.031, 0.022, 0.010
s_3^2	0.88	-1.23, -0.63, 0.30, 0.68
	0.025	0.007, 0.052, 0.018, 0.011
s_3^3	0.51	-1.02, 0.56, -0.42
	0.071	0.016, 0.004, 0.019

To properly estimate dynamics of the r_l^m , we would have to fit not only moments of the distribution of s_l^m , as we have done, but also all the dynamical statistics. However, this was infeasible and thus we are not able to make a serious estimate. Furthermore, statistics for individual cells were not well reproduced (Fig. 8). Thus, as an approximation, we resorted to using the dynamics of s_l^m multiplied by γ_l^m and for $m = 0$ adding δ_l . We ran simulations of this dynamics for r_l^m and calculated the corresponding s_l^m . The simulated covariance matrices are listed in Eqs. (51)–(53) (compare to Appendix A; however, values here are calculated using discrete time); they are roughly similar to the true values (this is also true for the angular momenta $L(v^i, v^j)$ and diffusivities, not shown), which indicates that we have a reasonable approximation. We then used the quadratic fit (Eqs. (44)–(50)) to calculate theoretically the terms in the third-order quantities up to quadratic order in β (i.e., combining α and β into a single linear coefficient when writing in terms of demeaned variables) under assumption of a linear Gaussian process for r_l^m , orientational changes, and velocity. We also ignore population heterogeneity. The advantage of the theoretical approach is that it decomposes the value into a sum of terms, thus allowing sensitivity to parameters to be more easily examined. In no case did a small quantity result from the subtraction of large quantities. On the other hand, simulation allows the full nonlinearity to be accounted for. Results from simulations were in line with theoretical estimates. This procedure gives a rough order-of-magnitude estimate for the contribution of nonlinear shape mapping to measured quantities.

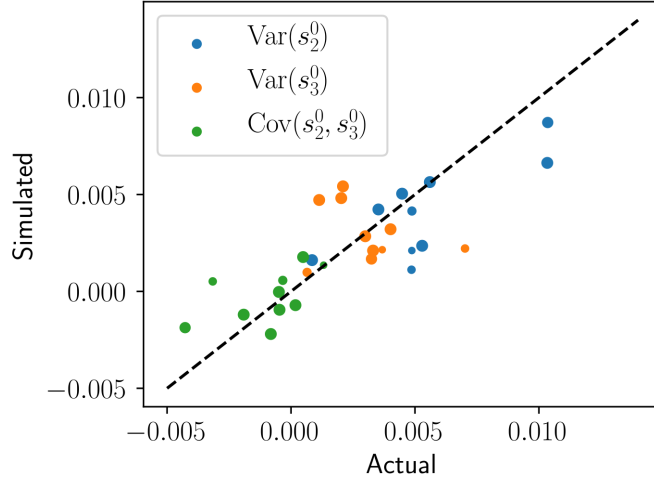


FIGURE 8. Variance and covariance for individual cells, actual and simulated. The size of the marker is proportional to the length of the time-series.

(51)

$$\mathbf{C}^0 = \begin{pmatrix} 3.8 \times 10^{-3} & -5.0 \times 10^{-4} & 0 & -1.4 \times 10^{-4} & 3.1 \times 10^{-3} \\ -5.0 \times 10^{-4} & 2.8 \times 10^{-3} & 1.4 \times 10^{-4} & 0 & -7.0 \times 10^{-4} \\ 0 & 1.4 \times 10^{-4} & 1.6 \times 10^{-4} & -1.3 \times 10^{-5} & -4.9 \times 10^{-4} \\ -1.4 \times 10^{-4} & 0 & -1.3 \times 10^{-5} & 1.6 \times 10^{-4} & -2.5 \times 10^{-4} \\ 3.1 \times 10^{-3} & -7.0 \times 10^{-4} & -4.9 \times 10^{-4} & -2.5 \times 10^{-4} & 0.041 \end{pmatrix}$$

(52)

$$\mathbf{C}^1 = \begin{pmatrix} 9.3 \times 10^{-3} & 1.0 \times 10^{-4} & 0 & -2.0 \times 10^{-4} & 1.3 \times 10^{-3} & 9.5 \times 10^{-3} \\ 1.0 \times 10^{-4} & 3.4 \times 10^{-3} & 2.0 \times 10^{-4} & 0 & -2.6 \times 10^{-4} & 4.0 \times 10^{-4} \\ 0 & 2.0 \times 10^{-4} & 2.4 \times 10^{-4} & -2.7 \times 10^{-5} & -1.2 \times 10^{-4} & 2.6 \times 10^{-4} \\ -2.0 \times 10^{-4} & 0 & -2.7 \times 10^{-5} & 2.4 \times 10^{-4} & 9.9 \times 10^{-5} & -9.4 \times 10^{-5} \\ 1.3 \times 10^{-3} & -2.6 \times 10^{-4} & -1.2 \times 10^{-4} & 9.9 \times 10^{-5} & 1.1 \times 10^{-3} & 4.9 \times 10^{-3} \\ 9.5 \times 10^{-3} & 4.0 \times 10^{-4} & 2.6 \times 10^{-4} & -9.4 \times 10^{-5} & 4.9 \times 10^{-3} & 0.064 \end{pmatrix}$$

(53)

$$\mathbf{C}^2 = \begin{pmatrix} 4.0 \times 10^{-3} & 2.7 \times 10^{-3} & 0 & -2.3 \times 10^{-5} \\ 2.7 \times 10^{-3} & 2.4 \times 10^{-3} & 2.4 \times 10^{-5} & 0 \\ 0 & 2.4 \times 10^{-5} & 9.2 \times 10^{-5} & 5.6 \times 10^{-5} \\ -2.3 \times 10^{-5} & 0 & 5.6 \times 10^{-5} & 7.6 \times 10^{-5} \end{pmatrix}$$

10. CODE AVAILABILITY

Code and data files are available at https://github.com/yeerenlow/tcells_paper_code.

REFERENCES

- [1] B. Alberts, A. Johnson, J. Lewis, D. Morgan, M. Raff, K. Roberts, and P. Walter. *Molecular Biology of the Cell*. Garland Science, 6 edition, 2015.
- [2] T. Lämmermann and M. Sixt. Mechanical modes of ‘amoeboid’ cell migration. *Curr. Opin. Cell Biol.*, 21:636–644, 2009.
- [3] J. Murray, H. Vawter-Hugart, E. Voss, and D. R. Soll. Three-dimensional motility cycle in leukocytes. *Cell Motil. Cytoskeleton*, 22:211–223, 1992.
- [4] A. Leithner, A. Eichner, J. Müller, A. Reversat, M. Brown, J. Schwarz, J. Merrin, D. J. J. de Gorter, F. Schur, J. Bayerl, I. de Vries, S. Wieser, R. Hauschild, F. P. L. Lai, M. Moser, D. Kerjaschki, K. Rottner, J. V. Small, T. E. B. Stradal, and M. Sixt. Diversified actin protrusions promote environmental exploration but are dispensable for locomotion of leukocytes. *Nat. Cell Biol.*, 18:1253–1259, 2016.
- [5] H. D. Moreau, M. Piel, R. Voituriez, and A.-M. Lennon-Duménil. Integrating physical and molecular insights on immune cell migration. *Trends Immunol.*, 39:632–643, 2018.
- [6] L. Dupré, R. Houmadi, C. Tang, and J. Rey-Barroso. T lymphocyte migration: an action movie starring the actin and associated actors. *Front. Immunol.*, 6:586, 2015.
- [7] H. D. Moreau, A.-M. Lennon-Duménil, and P. Pierobon. “If you please... draw me a cell”. Insights from immune cells. *J. Cell Sci.*, 133:jcs244806, 2020.
- [8] P. Friedl, S. Borgmann, and E.-B. Bröcker. Amoeboid leukocyte crawling through extracellular matrix: lessons from the *Dictyostelium* paradigm of cell movement. *J. Leukoc. Biol.*, 70:491–509, 2001.
- [9] P. Friedl and B. Weigelin. Interstitial leukocyte migration and immune function. *Nat. Immunol.*, 9:960–969, 2008.
- [10] E. K. Paluch, I. M. Aspalter, and M. Sixt. Focal adhesion-independent cell migration. *Annu. Rev. Cell Dev. Biol.*, 32:469–490, 2016.
- [11] P. Kameritsch and J. Renkawitz. Principles of leukocyte migration strategies. *Trends Cell Biol.*, 30:818–832, 2020.
- [12] A. D. Doyle, R. J. Petrie, M. L. Kutys, and K. M. Yamada. Dimensions in cell migration. *Curr. Opin. Cell Biol.*, 25:642–649, 2013.
- [13] K. M. Yamada and M. Sixt. Mechanisms of 3D cell migration. *Nat. Rev. Mol. Cell Biol.*, 20:738–752, 2019.
- [14] T. Lämmermann, B. L. Bader, S. J. Monkley, T. Worbs, R. Wedlich-Söldner, K. Hirsch, M. Keller, R. Förster, D. R. Critchley, R. Fässler, and M. Sixt. Rapid leukocyte migration by integrin-independent flowing and squeezing. *Nature*, 453:51–55, 2008.
- [15] A. Reversat, F. Gaertner, J. Merrin, J. Stopp, S. Tasciyan, J. Aguilera, I. de Vries, R. Hauschild, M. Hons, M. Piel, A. Callan-Jones, R. Voituriez, and M. Sixt. Cellular locomotion using environmental topography. *Nature*, 582:582–585, 2020.
- [16] M. F. Krummel, F. Bartumeus, and A. Gérard. T cell migration, search strategies and mechanisms. *Nat. Rev. Immunol.*, 16:193–201, 2016.
- [17] P. Mrass, J. Petravic, M. P. Davenport, and W. Weninger. Cell-autonomous and environmental contributions to the interstitial migration of T cells. *Semin. Immunopathol.*, 32:257–274, 2010.
- [18] W. Weninger, M. Biro, and R. Jain. Leukocyte migration in the interstitial space of non-lymphoid organs. *Nat. Rev. Immunol.*, 14:232–246, 2014.
- [19] M. A. Munoz, M. Biro, and W. Weninger. T cell migration in intact lymph nodes *in vivo*. *Curr. Opin. Cell Biol.*, 30:17–24, 2014.
- [20] A. Gérard, G. Patino-Lopez, P. Beemiller, R. Nambiar, K. Ben-Aissa, Y. Liu, F. J. Totah, M. J. Tyska, S. Shaw, and M. F. Krummel. Detection of rare antigen-presenting cells through T cell-intrinsic meandering motility, mediated by Myo1g. *Cell*, 158:492–505, 2014.
- [21] P. Mrass, S. R. Oruganti, G. M. Fricke, J. Tafoya, J. R. Byrum, L. Yang, S. L. Hamilton, M. J. Miller, M. E. Moses, and J. L. Cannon. ROCK regulates the intermittent mode of interstitial T cell migration in inflamed lungs. *Nat. Commun.*, 8:1010, 2017.
- [22] J. Allard and A. Mogilner. Traveling waves in actin dynamics and cell motility. *Curr. Opin. Cell Biol.*, 25:107–115, 2013.
- [23] N. Inagaki and H. Katsuno. Actin waves: origin of cell polarization and migration? *Trends Cell Biol.*, 27:515–526, 2017.

- [24] S. Saha, T. L. Nagy, and O. D. Weiner. Joining forces: crosstalk between biochemical signalling and physical forces orchestrates cellular polarity and dynamics. *Phil. Trans. R. Soc. B*, 373:20170145, 2018.
- [25] J. Kuhn, Y. Lin, and P. N. Devreotes. Using live-cell imaging and synthetic biology to probe directed migration in *Dictyostelium*. *Front. Cell Dev. Biol.*, 9:740205, 2021.
- [26] C. Shi and P. A. Iglesias. Excitable behavior in amoeboid chemotaxis. *WIREs Syst. Biol. Med.*, 5:631–642, 2013.
- [27] X. Li, Y. Miao, D. S. Pal, and P. N. Devreotes. Excitable networks controlling cell migration during development and disease. *Semin. Cell Dev. Biol.*, 100:133–142, 2020.
- [28] D. S. Pal, X. Li, T. Banerjee, Y. Miao, and P. N. Devreotes. The excitable signal transduction networks: movers and shapers of eukaryotic cell migration. *Int. J. Dev. Biol.*, 63:407–416, 2019.
- [29] Y. Cheng, B. Felix, and H. G. Othmer. The roles of signaling in cytoskeletal changes, random movement, direction-sensing and polarization of eukaryotic cells. *Cells*, 9:1437, 2020.
- [30] A. Buttenschön and L. Edelstein-Keshet. Bridging from single to collective cell migration: a review of models and links to experiments. *PLoS Comput. Biol.*, 16:e1008411, 2020.
- [31] M. Sun and M. H. Zaman. Modeling, signaling and cytoskeleton dynamics: integrated modeling-experimental frameworks in cell migration. *WIREs Syst. Biol. Med.*, 9:e1365, 2017.
- [32] S. Banerjee, M. L. Gardel, and U. S. Schwarz. The actin cytoskeleton as an active adaptive material. *Annu. Rev. Condens. Matter Phys.*, 11:421–439, 2020.
- [33] W. R. Holmes and L. Edelstein-Keshet. A comparison of computational models for eukaryotic cell shape and motility. *PLoS Comput. Biol.*, 8:e1002793, 2012.
- [34] A. Callan-Jones. Self-organization in amoeboid motility. *Front. Cell Dev. Biol.*, 10:1000071, 2022.
- [35] G. Danuser, J. Allard, and A. Mogilner. Mathematical modeling of eukaryotic cell migration: insights beyond experiments. *Annu. Rev. Cell Dev. Biol.*, 29:501–528, 2013.
- [36] B. Stinner and T. Bretschneider. Mathematical modelling in cell migration: tackling biochemistry in changing geometries. *Biochem. Soc. Trans.*, 48:419–428, 2020.
- [37] K. DiNapoli, D. N. Robinson, and P. A. Iglesias. Tools for computational analysis of moving boundary problems in cellular mechanobiology. *WIREs Mech. Dis.*, 13:e1514, 2021.
- [38] E. J. Campbell and P. Bagchi. A computational model of amoeboid cell swimming. *Phys. Fluids*, 29:101902, 2017.
- [39] N. P. Barry and M. S. Bretscher. *Dictyostelium* amoebae and neutrophils can swim. *Proc. Natl. Acad. Sci. U.S.A.*, 107:11376–11380, 2010.
- [40] A. J. Bae and E. Bodenschatz. On the swimming of *Dictyostelium* amoebae. *Proc. Natl. Acad. Sci. U.S.A.*, 107:E165–E166, 2010.
- [41] P. J. M. van Haastert. Amoeboid cells use protrusions for walking, gliding and swimming. *PLoS ONE*, 6:e27532, 2011.
- [42] M. K. Driscoll, C. McCann, R. Kopace, T. Homan, J. T. Fourkas, C. Parent, and W. Losert. Cell shape dynamics: from waves to migration. *PLoS Comput. Biol.*, 8:e1002392, 2012.
- [43] E. M. Purcell. Life at low Reynolds number. *AIP Conf. Proc.*, 28:49–64, 1976.
- [44] A. Farutin, J. Étienne, C. Misbah, and P. Recho. Crawling in a fluid. *Phys. Rev. Lett.*, 123:118101, 2019.
- [45] H. G. Othmer. Eukaryotic cell dynamics from crawlers to swimmers. *WIREs Comput. Mol. Sci.*, 9:e1376, 2018.
- [46] A. L. Godeau, M. Leoni, J. Comelles, T. Guyomar, M. Lieb, H. Delanoë-Ayari, A. Ott, S. Harlepp, P. Sens, and D. Riveline. 3D single cell migration driven by temporal correlation between oscillating force dipoles. *eLife*, page 71032, 2022.
- [47] D. L. Bodor, W. Pönisch, R. G. Endres, and E. K. Paluch. Of cell shapes and motion: the physical basis of animal cell migration. *Dev. Cell*, 52:550–562, 2020.
- [48] U. S. Schwarz and M. Vicente-Manzanares. Cell mechanics and mechanobiology. *Eur. J. Cell Biol.*, 102:151304, 2023.
- [49] L. Li, E. C. Cox, and H. Flyvbjerg. “Dicty dynamics”: *Dictyostelium* motility as persistent random motion. *Phys. Biol.*, 8:046006, 2011.
- [50] D. Selmeczi, L. Li, L. I. I. Pedersen, S. F. Nørrelykke, P. H. Hagedorn, S. Mosler, N. B. Larsen, E. C. Cox, and H. Flyvbjerg. Cell motility as random motion: a review. *Eur. Phys. J.: Spec. Top.*, 157:1–15, 2008.
- [51] L. Li, S. Nørrelykke, and E. C. Cox. Persistent cell motion in the absence of external signals: a search strategy for eukaryotic cells. *PLoS ONE*, 3:e2093, 2008.
- [52] H. U. Bödeker, C. Beta, T. D. Frank, and E. Bodenschatz. Quantitative analysis of random ameoboid motion. *EPL*, 90:28005, 2010.

- [53] G. Amselem, M. Theves, A. Bae, E. Bodenschatz, and C. Beta. A stochastic description of *Dictyostelium* chemotaxis. *PLoS ONE*, 7:e37213, 2012.
- [54] L. Bosgraaf and P. J. M. van Haastert. The ordered extension of pseudopodia by amoeboid cells in the absence of external cues. *PLoS ONE*, 4:e5253, 2009.
- [55] P. J. M. van Haastert. A model for a correlated random walk based on the ordered extension of pseudopodia. *PLoS Comput. Biol.*, 6:e1000874, 2010.
- [56] P. J. M. van Haastert. A stochastic model for chemotaxis based on the ordered extension of pseudopods. *Biophys. J.*, 99:3345–3354, 2010.
- [57] P. J. M. van Haastert. Unified control of amoeboid pseudopod extension in multiple organisms by branched F-actin in the front and parallel F-actin/myosin in the cortex. *PLoS ONE*, 15:e0243442, 2020.
- [58] P. J. M. van Haastert. Short- and long-term memory of moving amoeboid cells. *PLoS ONE*, 16:e0246345, 2021.
- [59] X. Liu, E. S. Welf, and J. M. Haugh. Linking morphodynamics and directional persistence of T lymphocyte migration. *J. R. Soc. Interface*, 12:20141412, 2015.
- [60] C. Metzner, C. Mark, J. Steinwachs, L. Lautscham, F. Stadler, and B. Fabry. Superstatistical analysis and modelling of heterogeneous random walks. *Nat. Commun.*, 6:7516, 2015.
- [61] A. G. Cherstvy, O. Nagel, C. Beta, and R. Metzler. Non-Gaussianity, population heterogeneity, and transient superdiffusion in the spreading dynamics of amoeboid cells. *Phys. Chem. Chem. Phys.*, 20:23034–23054, 2018.
- [62] B. G. Mitterwallner, C. Schreiber, J. O. Daldrop, J. O. Rädler, and R. R. Netz. Non-Markovian data-driven modeling of single-cell motility. *Phys. Rev. E*, 101:032408, 2020.
- [63] G. J. Stephens, B. Johnson-Kerner, W. Bialek, and W. S. Ryu. Dimensionality and dynamics in the behavior of *C. elegans*. *PLoS Comput. Biol.*, 4:e1000028, 2008.
- [64] G. J. Stephens, B. Johnson-Kerner, W. Bialek, and W. S. Ryu. From modes to movement in the behavior of *Caenorhabditis elegans*. *PLoS ONE*, 5:e13914, 2010.
- [65] G. J. Stephens, M. Bueno de Mesquita, W. S. Ryu, and W. Bialek. Emergence of long timescales and stereotyped behaviors in *Caenorhabditis elegans*. *Proc. Natl. Acad. Sci. U.S.A.*, 108:7286–7289, 2011.
- [66] A. E. X. Brown, E. I. Yemini, L. J. Grundy, T. Jucikas, and W. R. Schafer. A dictionary of behavioral motifs reveals clusters of genes affecting *Caenorhabditis elegans* locomotion. *Proc. Natl. Acad. Sci. U.S.A.*, 110:791–796, 2012.
- [67] E. Yemini, T. Jucikas, L. J. Grundy, A. E. X. Brown, and W. R. Schafer. A database of *Caenorhabditis elegans* behavioral phenotypes. *Nat. Methods*, 10:877–879, 2013.
- [68] A. Gomez-Marin, G. J. Stephens, and A. E. X. Brown. Hierarchical compression of *Caenorhabditis elegans* locomotion reveals phenotypic differences in the organization of behaviour. *J. R. Soc. Interface*, 13:20160466, 2016.
- [69] A. Javer, L. Ripoll-Sánchez, and A. E. X. Brown. Powerful and interpretable behavioural features for quantitative phenotyping of *Caenorhabditis elegans*. *Phil. Trans. R. Soc. B*, 373:20170375, 2018.
- [70] B. C. Daniels, W. S. Ryu, and I. Nemenman. Automated, predictive, and interpretable inference of *Caenorhabditis elegans* escape dynamics. *Proc. Natl. Acad. Sci. U.S.A.*, 116:7226–7231, 2019.
- [71] A. C. Costa, T. Ahamed, and G. J. Stephens. Adaptive, locally linear models of complex dynamics. *Proc. Natl. Acad. Sci. U.S.A.*, 116:1501–1510, 2019.
- [72] T. Ahamed, A. C. Costa, and G. J. Stephens. Capturing the continuous complexity of behaviour in *Caenorhabditis elegans*. *Nat. Phys.*, 17:275–283, 2021.
- [73] A. C. Costa, T. Ahamed, D. Jordan, and G. J. Stephens. Maximally predictive states: from partial observations to long timescales. *Chaos*, 33:023136, 2023.
- [74] D. B. Brückner, A. Fink, C. Schreiber, P. J. F. Röttgermann, J. O. Rädler, and C. P. Broedersz. Stochastic nonlinear dynamics of confined cell migration in two-state systems. *Nat. Phys.*, 15:595–601, 2019.
- [75] D. B. Brückner, A. Fink, J. O. Rädler, and C. P. Broedersz. Disentangling the behavioural variability of confined cell migration. *J. R. Soc. Interface*, 17:20190689, 2020.
- [76] A. Fink, D. B. Brückner, C. Schreiber, P. J. F. Röttgermann, C. P. Broedersz, and J. O. Rädler. Area and geometry dependence of cell migration in asymmetric two-state micropatterns. *Biophys. J.*, 118:552–564, 2020.
- [77] D. B. Brückner, N. Arit, A. Fink, P. Ronceray, J. O. Rädler, and C. P. Broedersz. Learning the dynamics of cell–cell interactions in confined cell migration. *Proc. Natl. Acad. Sci. U.S.A.*, 118:e2016602118, 2021.
- [78] D. B. Brückner, M. Schmitt, A. Fink, G. Ladurner, J. Flommersfeld, N. Arit, E. Hannezo, J. O. Rädler, and C. P. Broedersz. Geometry adaptation of protrusion and polarity dynamics in confined cell migration. *Phys. Rev. X*, 12:031041, 2022.

- [79] David B. Brückner and Chase P. Broedersz. Learning dynamical models of single and collective cell migration: a review, 2023.
- [80] H. Cavanagh, D. Kempe, J. K. Mazalo, M. Biro, and R. G. Endres. T cell morphodynamics reveal periodic shape oscillations in three-dimensional migration. *J. R. Soc. Interface*, 19:20220081, 2022.
- [81] P. Friedl, F. Entschladen, C. Conrad, B. Niggemann, and K. S. Zänker. CD4⁺ T lymphocytes migrating in three-dimensional collagen lattices lack focal adhesions and utilize β 1 integrin-independent strategies for polarization, interaction with collagen fibers and locomotion. *Eur. J. Immunol.*, 28:2331–2343, 1998.
- [82] K. Keren, Z. Pincus, G. M. Allen, E. L. Barnhart, G. Marriott, A. Mogilner, and J. A. Theriot. Mechanism of shape determination in motile cells. *Nature*, 453:475–480, 2008.
- [83] A. Farutin, S. Rafai, D. K. Dysthe, A. Duperray, P. Peyla, and C. Misbah. Amoeboid swimming: a generic self-propulsion of cells in fluids by means of membrane deformations. *Phys. Rev. Lett.*, 111:228102, 2013.
- [84] A. Frishman and P. Ronceray. Learning force fields from stochastic trajectories. *Phys. Rev. X*, 10:021009, 2020.
- [85] D. B. Brückner, P. Ronceray, and C. P. Broedersz. Inferring the dynamics of underdamped stochastic systems. *Phys. Rev. Lett.*, 125:058103, 2020.
- [86] L. Tweedy, P. Witzel, D. Heinrich, R. H. Insall, and R. G. Endres. Screening by changes in stereotypical behavior during cell motility. *Sci. Rep.*, 9:8784, 2019.
- [87] Y. I. Low. Second- and third-order properties of multidimensional Langevin equations, 2023.
- [88] B. Efron and R. J. Tibshirani. *An Introduction to the Bootstrap*. Chapman & Hall/CRC, 1994.
- [89] U. Seifert. From stochastic thermodynamics to thermodynamic inference. *Annu. Rev. Condens. Matter Phys.*, 10:171–192, 2019.
- [90] P.-H. Wu, A. Giri, S. X. Sun, and D. Wirtz. Three-dimensional cell migration does not follow a random walk. *Proc. Natl. Acad. Sci.*, 111:3949–3954, 2014.
- [91] T. Kwon, O.-S. Kwon, H.-J. Cha, and B. J. Sung. Stochastic and heterogeneous cancer cell migration: theory and experiment. *Sci. Rep.*, 9:16297, 2019.